Gamma-Ray Spectroscopy: A Comprehensive Investigation

Samyak Tiwari

December 20, 2024

Abstract

This report delves into the core principles and practical applications of gamma-ray spectroscopy, employing a NaI(Tl) scintillation detector. The experiment encompasses calibration with radioactive sources, validation of the inverse-square law of radiation intensity, and determination of mass attenuation coefficients for various materials. Results affirm theoretical expectations and highlight the significance of gamma-ray interactions.

Table of Contents

1 Introduction

Gamma-ray spectroscopy serves as a pivotal tool in nuclear physics for exploring nuclear energy states. By detecting high-energy photons emitted during nuclear transitions, this technique provides profound insights into the structural and dynamic properties of atomic nuclei. The experiment emphasizes the use of a thallium-doped sodium iodide [NaI(Tl)] detector to analyze gamma-ray energy spectra.

Theory

Gamma Rays and Their Interactions

Gamma rays are high-energy photons emitted during nuclear transitions, carrying no charge but having considerable penetrating power. They interact with matter through various mechanisms, primarily the photoelectric effect, Compton scattering, and pair production.

Photoelectric Effect: In this process, a gamma photon transfers its energy to an atomic electron, ejecting it from its orbital. The probability of this interaction is higher at lower gamma-ray energies and with materials of higher atomic number.

Compton Scattering: Compton scattering occurs when a gamma photon interacts with a loosely bound or free electron, transferring part of its energy and changing direction. The energy of the scattered photon is described by:

$$E'_\gamma = \frac{E_\gamma}{1 + \frac{E_\gamma}{m_e c^2}(1 - \cos\theta)}$$

where E_γ is the initial photon energy, E'_γ is the energy after scattering, m_e is the electron mass, c is the speed of light, and θ is the scattering angle. The Compton edge marks the maximum energy transfer to an electron, occurring at a scattering angle of 180°.

Scintillation Effect

The scintillation process is integral to gamma-ray detection in this experiment. When gamma rays interact with the thallium-doped sodium iodide (NaI(Tl)) crystal, the energy deposited excites electrons in the material. These electrons subsequently de-excite, emitting photons in the visible spectrum. The light output is proportional to the energy of the incident gamma photon. A photomultiplier tube (PMT) amplifies the light signal, converting it into measurable electrical pulses.

Mass Attenuation Coefficient

The mass attenuation coefficient quantifies a material's capability to attenuate gamma rays. It is calculated as:

$$\mu/\rho = \frac{\ln(I_0/I)}{t\rho}$$

where μ is the linear attenuation coefficient, ρ is the material's density, I_0 is the initial intensity of gamma rays, I is the transmitted intensity, and t is the material's thickness. This parameter provides insight into how effectively a material absorbs gamma radiation.

Inverse-Square Law

The intensity of gamma radiation diminishes with the square of the distance from the source, as described by the inverse-square law:

$$I \propto \frac{1}{d^2}$$

where I is the radiation intensity and d is the distance from the source. This relationship is verified in the experiment by measuring the detector's response at various distances, confirming that the gamma-ray intensity decreases with increasing separation from the source.

2 Experimental Setup and Methodology

2.1 Apparatus

The experimental arrangement for gamma-ray spectroscopy is designed to study gamma-ray interactions and includes the following key components:

1. **NaI(Tl) Detector** The primary detector is a thallium-doped sodium iodide (NaI(Tl)) crystal with dimensions of 3 inches in diameter and height. This detector is highly responsive to gamma rays, producing visible light when gamma photons interact with the material.

2. **Photomultiplier Tube (PMT)** Coupled to the NaI(Tl) crystal, the PMT (e.g., ORTEC 905-4) converts light emitted by the scintillator into electrical pulses. It includes a photocathode for photon-to-electron conversion, a series of dynodes to amplify the electrons, and an anode for collecting the final amplified signal.

3. **High-Voltage Power Supply** A stable high-voltage power supply (e.g., Stanford Research Systems PS325) powers the PMT, typically operating in the range of 400–800 V. This ensures optimal PMT gain for precise signal detection.

4. **Pulse Height Analyzer (PHA)** The analyzer digitizes the PMT output and displays a histogram of pulse heights corresponding to gamma-ray energy spectra. It integrates a National Instruments NI-5124 digitizer card and LabVIEW software for real-time spectrum acquisition and visualization.

5. **Spectroscopy Amplifier** The amplifier processes the electrical signals from the PMT by adjusting their shape and strength. Coarse and fine gain settings allow optimization of signal amplification while minimizing noise.

6. **Radioactive Sources** Common radioactive sources include ^{137}Cs, ^{60}Co, and ^{22}Na. These are used due to their well-documented emission energies for calibration and analysis.

7. **Lead Shielding and Collimators** Lead bricks surround the detector and sources to reduce background radiation. Collimators are used to direct gamma rays from the source to the detector, enhancing precision in measurement.

8. **Geiger Counter and Safety Equipment** A Geiger counter monitors radiation levels in the laboratory. Experimenters must wear gloves and radiation monitoring rings when handling radioactive materials to maintain safety.

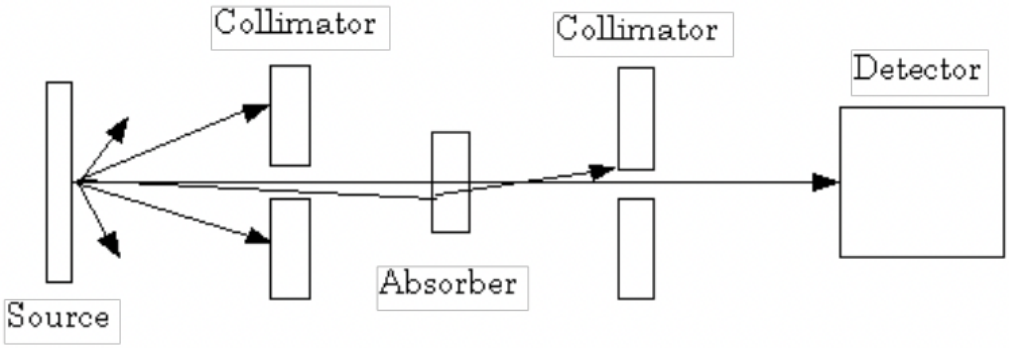

Figure 13: A diagram of Gamma-ray Spectroscopy

Figure 1: Setup from lab manual.[1]

2.2 Procedure

The experimental procedure is detailed as follows:

1. **Initial Setup** Inspect all equipment for proper functioning. Securely mount the NaI(Tl) detector and connect the PMT to the high-voltage power supply, amplifier, and pulse height analyzer.

2. **Calibration** Activate the high-voltage power supply and set it to an initial value, such as 700 V. Adjust the amplifier's coarse and fine gain settings to optimize signal clarity. Verify the system by observing initial spectra on the PHA and adjust settings to minimize noise.

3. **Background Measurement** Record a spectrum without a radioactive source to measure background radiation. Use lead shielding to reduce interference. Subtract the background spectrum from subsequent measurements for accurate results.

4. **Placement of Radioactive Source** Carefully position a radioactive source in front of the detector at a specific distance (e.g., 30 cm). Align the source, collimator, and detector to ensure proper gamma-ray direction.

5. **Data Collection** Initiate data acquisition on the PHA. Adjust the sampling rate, gain, and range to capture all spectral features. Collect data for a live time of 100–150 seconds to ensure statistical significance.

6. **Variation in Source and Distance** Conduct measurements for different radioactive sources to study spectral differences. For the inverse-square law verification, vary the distance between the source and detector and record the intensity for each position.

7. **Spectral Analysis** Analyze the spectra to identify features such as photopeaks, Compton edges, and backscatter peaks. Fit Gaussian curves to determine peak energies and widths, and calculate the detector's energy resolution.

8. **Measurement of Mass Attenuation Coefficients** Place materials like aluminum, copper, or lead with known thicknesses between the source and detector. Record the transmitted gamma-ray intensity and calculate the mass attenuation coefficient using the formula:

$$\mu/\rho = \frac{\ln(I_0/I)}{t\rho}$$

Repeat this process for multiple thicknesses and compare results with theoretical values.

9. **Safety Measures and Shutdown** Return radioactive sources to secure storage after completing data collection. Turn off equipment systematically in reverse order of initialization. Verify ambient radiation levels with a Geiger counter.

10. **Data Analysis** Export raw data from the PHA for further analysis. Use computational tools to process spectra, subtract background noise, and calculate parameters such as resolution, peak widths, and mass attenuation coefficients.

3 Equipment Calibration

3.1 Relative Gain of Photomultiplier Tube

This section investigates how varying the high voltage applied to the photomultiplier tube (PMT) affects its gain. The experiment focused on capturing spectra for the ^{137}Cs source under different high voltage settings. The equipment settings used for this experiment are summarized in Table 1. Voltages below 600 V produced weak or unreliable signals, while settings above 800 V resulted in excessive peak broadening, making them unsuitable for precise measurements.

Table 1: PMT Gain Experiment Settings

Parameter	**Value**
Amplifier Gain	100
Pulse Height Analyzer Gain	2.5

3.1.1 Relationship Between PMT High Voltage and Peak Voltage

The data collected include the peak voltages for different high voltage settings applied to the PMT, as shown in Table 2. The experiment demonstrates an exponential relationship between the PMT gain and the applied high voltage, as expected.

Figure 2 illustrates the relationship between the PMT high voltage and the ^{137}Cs peak voltage. The data show that as the high voltage increases, the peak voltage rises exponentially, indicating the proportional relationship between PMT gain and the applied voltage.

Table 2: Peak Voltages for Given PMT High Voltage

PMT High Voltage (V)	Peak Voltage (V)
600	0.21
620	0.27
640	0.35
660	0.44
680	0.57
700	0.72
720	0.90
740	1.10
760	1.38
780	1.71
800	2.15

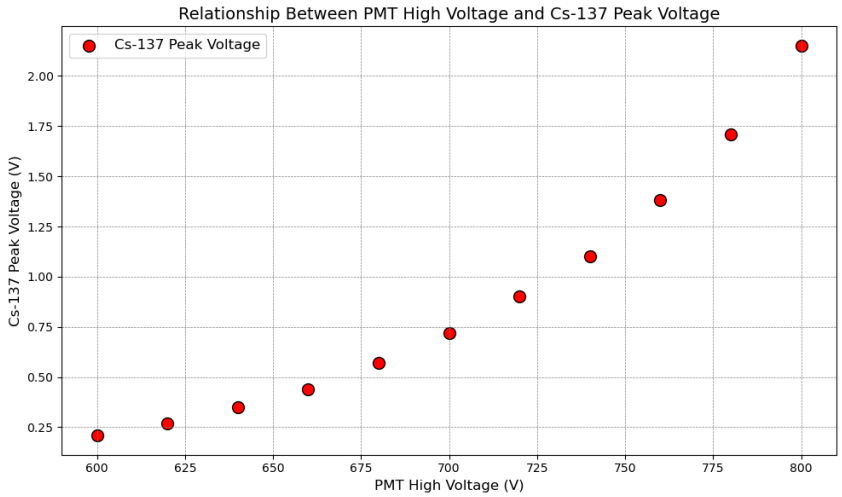

Figure 2: Relationship Between PMT High Voltage and ^{137}Cs Peak Voltage.

3.1.2 Power-Law Fit

To quantify the relationship, the data were fitted to a power-law model of the form:

$$G = \alpha V^{\beta}$$

where G represents the gain, V is the PMT high voltage, and α and β are fitting parameters. The best-fit curve and the corresponding data points are shown in Figure 3.

The fitted equation for the gain is:

$$G = (3.422 \pm 0.024) \times 10^{-24} V^{8.196 \pm 0.078}$$

The results align well with theoretical expectations. However, voltages above 800 V resulted in excessive peak broadening, and settings below 600 V yielded weak signals. A PMT high voltage of 780 V was determined to be optimal for balancing signal sharpness and resolution.

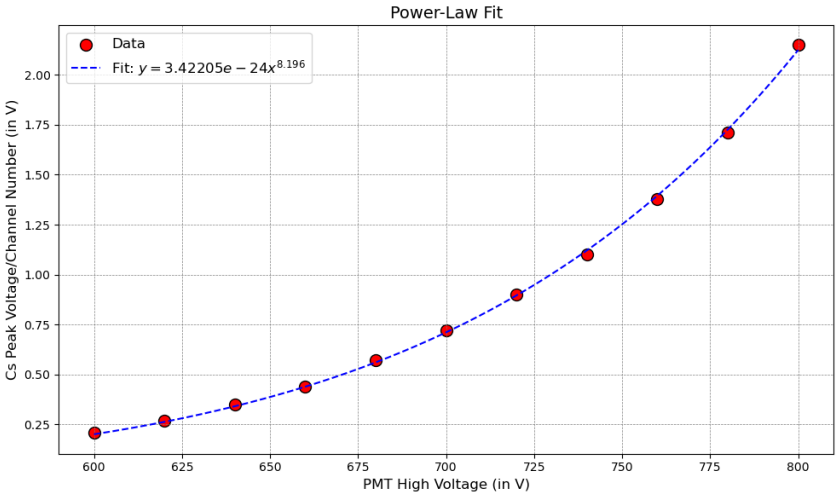

Figure 3: Power-Law Fit: ^{137}Cs Peak Voltage vs PMT High Voltage.

3.2 Identifying Linear Amps for Multiple Gains

To investigate linearity, several amplifier gain settings were analyzed, including 20, 40, and 300. At each gain setting, the input pulse amplitude was varied, and the corresponding peak voltages were recorded. This section examines the linear behavior of the amplifier at these different gains.

3.2.1 Gain 20

The amplifier gain was set to 20, and the input signal was incrementally increased to examine the linearity of the output response. At this gain setting, the amplifier displayed near-perfect linear behavior, as shown in Figure 4. The peak voltages increased proportionally with the input amplitudes, indicating that the amplifier was operating well within its linear range.

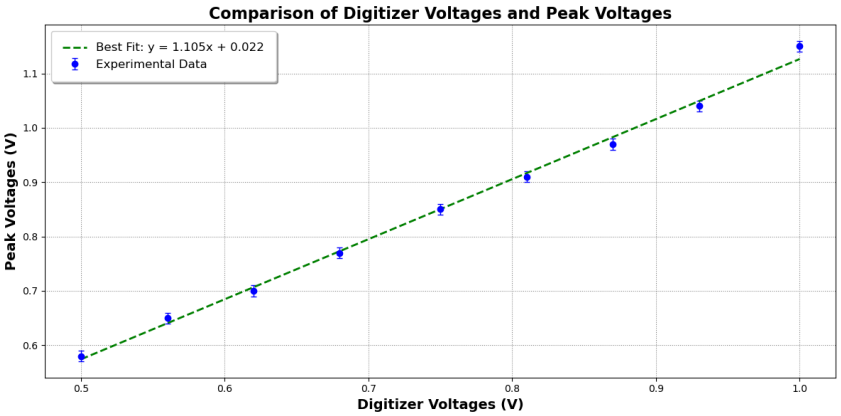

Figure 4: Peak voltage versus input amplitude for gain 20. The linear relationship demonstrates the amplifier's stable operation at this setting.

3.2.2 Gain 40

At a gain setting of 40, the amplifier continued to exhibit linear behavior across most of the input amplitude range. However, as the input amplitude approached the upper limit of the digitizer's range, slight deviations from linearity began to emerge. These deviations are likely due to the amplifier nearing its clipping threshold. Figure 5 illustrates this behavior.

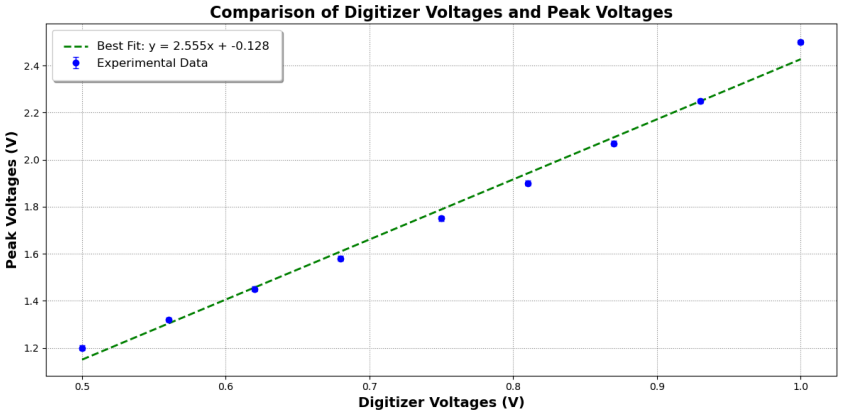

Figure 5: Peak voltage versus input amplitude for gain 40. Minor deviations from linearity are visible near the upper range of the digitizer.

3.2.3 Gain 300

At a gain setting of 300, significant non-linear behavior was observed as the input amplitude approached the digitizer's limits. Clipping occurred at lower input amplitudes compared to the previous settings, resulting in a distorted response. This behavior is illustrated in Figure 6, where the peak voltages no longer scale linearly with the input amplitudes. This demonstrates that the amplifier is operating outside its linear range at high gains.

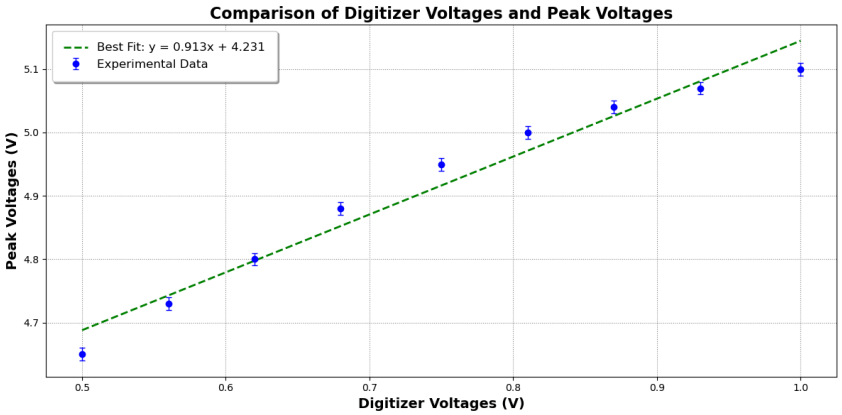

Figure 6: Peak voltage versus input amplitude for gain 300. The non-linear response and clipping are clearly visible.

3.2.4 Discussion

From these observations, it is evident that amplifier linearity is highly dependent on the gain setting. Lower gains, such as 20, allow for a wide linear range with minimal distortion. As the gain increases, the amplifier's linear range narrows, and clipping occurs at lower input amplitudes. These findings highlight the importance of selecting appropriate gain settings to maintain signal integrity and avoid distortion during data acquisition.

3.3 Clipping at Higher Gains

At higher amplifier gain settings, such as 300, clipping becomes a significant issue. Clipping occurs when the input signal exceeds the maximum voltage that the amplifier or digitizer can handle. This results in distortion of the recorded spectrum, where peaks appear flattened or split due to the inability of the system to process signals beyond its threshold.

This distortion not only affects the peak shape but also artificially increases the measured peak width. Consequently, the recorded channel numbers no longer correspond accurately to the true signal amplitudes, leading to errors in data interpretation. Clipping is particularly problematic for high-resolution measurements, where precise peak identification and analysis are essential.

Another effect of clipping is the introduction of low-energy artifacts in the spectrum. These artifacts are caused by baseline stabilization issues in the signal processing electronics, which incorrectly register spurious counts at lower energies. Such distortions can significantly skew the spectrum and complicate data analysis.

To mitigate these issues, it is essential to operate the amplifier within its linear range. For a gain setting of 300, this involves limiting the input signal amplitude to well below the clipping threshold. Additionally, increasing the sampling rate can help the digitizer process signals more accurately, reducing the severity of clipping.

3.4 Signal Pileup

Signal pileup occurs when multiple pulses arrive at the detector in rapid succession, overwhelming the electronics and causing errors in the recorded spectrum. This phenomenon is particularly evident when the repetition rate of the incoming signal exceeds the processing capacity of the detector and its associated electronics. As a result, multiple pulses can overlap and be interpreted as a single event, leading to skewed measurements and degraded energy resolution.

At high repetition rates, such as 16 kHz, pileup becomes a significant issue. Figure 7 illustrates the spectrum recorded at this repetition rate. The distortion of peaks is evident, with a broadening and splitting effect caused by the overlapping signals. These overlapping events introduce inaccuracies in the energy calibration, making it difficult to distinguish between true single-pulse events and pileup artifacts.

3.4.1 Causes and Implications of Pileup

The primary cause of pileup is the limited recovery time of the electronics, which prevents them from fully processing one pulse before the next arrives. This can happen when:

- The repetition rate of incoming pulses exceeds the system's processing capacity.

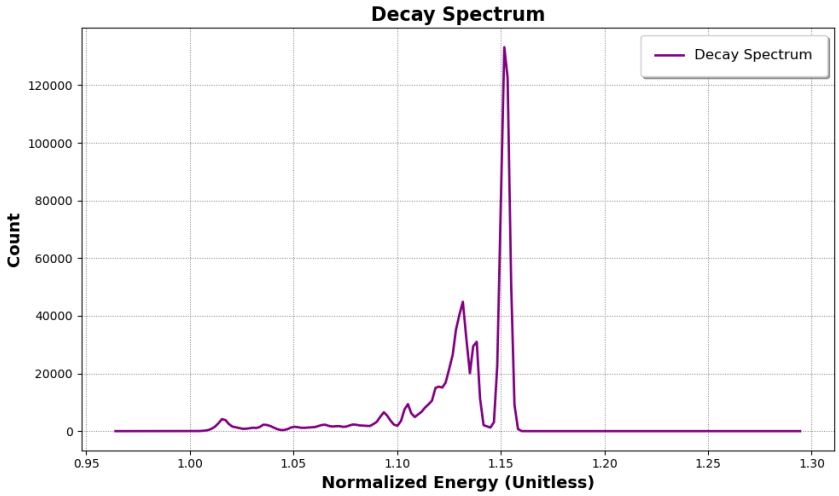

Figure 7: Spectrum for Simulated Digitizer Signal at 16 kHz Repetition Rate. Distortion and broadening of peaks due to signal pileup are clearly visible.

- The detector is placed too close to the source, resulting in an excessively high signal rate.

Pileup causes loss of accuracy: The total count and energy calibration are affected, reducing the reliability of the results.

To reduce the effects of pileup, several strategies can be employed:

- **Optimizing Repetition Rate:** Keeping the repetition rate within the detector's processing capabilities minimizes pileup.
- **Adjusting Detector Placement:** Increasing the distance between the detector and the source reduces the pulse rate, allowing for more accurate measurements.
- **Improving Electronics:** Utilizing faster electronics with shorter recovery times can help the system handle higher pulse rates more effectively.

3.5 Final Calibration Settings

The final calibration settings were chosen to ensure optimal performance of the detector system while minimizing errors and maximizing resolution. These settings were determined based on the analysis of gain linearity, signal pileup, and the operating ranges of the electronics. Table 3 summarizes the selected calibration parameters.

3.5.1 Justification of Settings

1. PMT High Voltage (780 V): - This setting provides sufficient amplification for detecting gamma-ray signals while avoiding excessive peak broadening and non-linearity.

2. Amplifier Gain (40): - A gain of 40 was chosen as it balances signal strength with linearity, ensuring that peaks are accurately recorded without distortion or clipping.

3. PHA Gain and Range (9 and 5 V): - These settings allow the spectra to span the entire range of the PHA, ensuring that the highest energy peak is recorded at the very edge of the spectrum without exceeding the digitizer limits.

Table 3: Final Calibration Settings

Parameter	**Value**
PMT High Voltage	780 V
Amplifier Gain	40
PHA Gain	9
PHA Range	5 V
PHA Sampling Rate	11 MHz
Live Time	60 s

4. PHA Sampling Rate (11 MHz): - The sampling rate was set to 11 MHz to accurately capture the pulses and reduce noise, especially at higher repetition rates.

5. Live Time (60 s): - A live time of 60 seconds was chosen to collect statistically significant data while keeping acquisition time reasonable.

These calibration settings were used consistently throughout the experiment to ensure reproducibility and accuracy in all measurements.

3.6 Background

With the calibrated setup, we began by taking background measurements. I subtracted the mean of Background 1 and Background 2 from all measurement data collected in this experiment. In particular, Background 3 had a spike that did not seem representative of the backgrounds we'd have while collecting data. This approach ensured that the backgrounds used for correction were more representative of the experimental conditions.

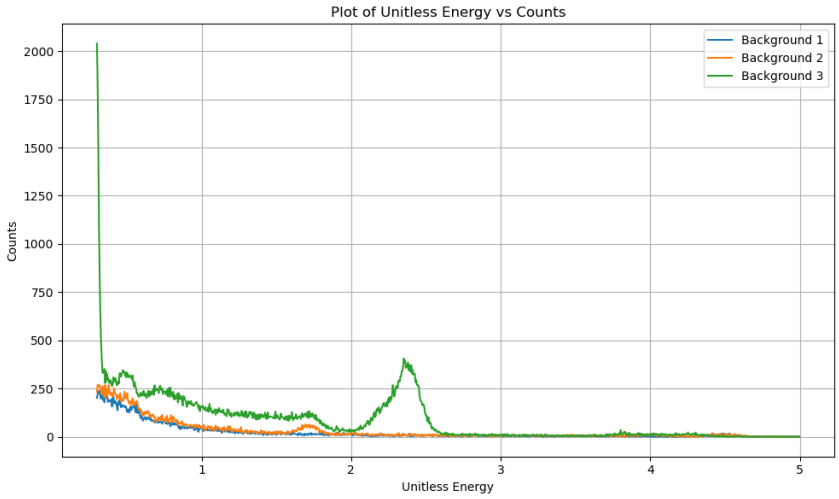

Figure 8: Three background PHA plots.

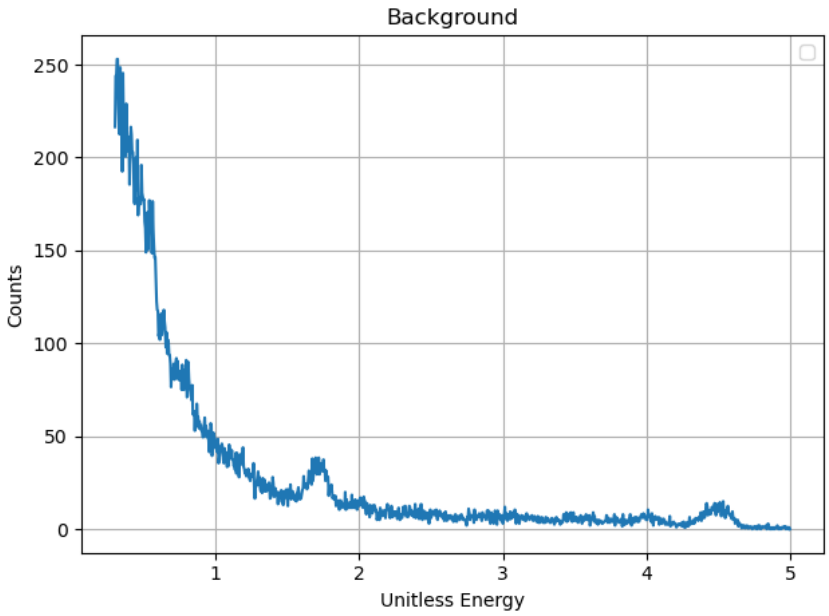

Figure 9: Final background used.

4 Trying our settings on some radiation spectra!

Let's walk through an example of fitting a Gaussian to a sodium spectrum!

The process of analyzing the data and extracting meaningful results involves several critical steps. This section outlines the steps taken to process the raw data, fit Gaussians to the identified peaks, and combine the fits for further analysis.

4.1 Removing Background Features

Raw data often contains background features that can obscure the peaks of interest. The first step in our analysis involves removing these background features to isolate the true signal. This was achieved by subtracting a smooth baseline function fitted to the background regions of the spectrum. The cleaned spectrum, free of background interference, is shown in Figure 10.

4.2 Fitting Gaussian Functions to Isolated Peaks

After the background is removed, individual peaks in the spectrum are identified and isolated by visual inspection. Each peak is then fitted with a Gaussian function of the form:

$$f(x) = a \exp\left(-\frac{(x-b)^2}{2c^2}\right)$$

where:

- a is the amplitude of the Gaussian,
- b is the mean or the center of the peak,
- c is the standard deviation, related to the width of the peak.

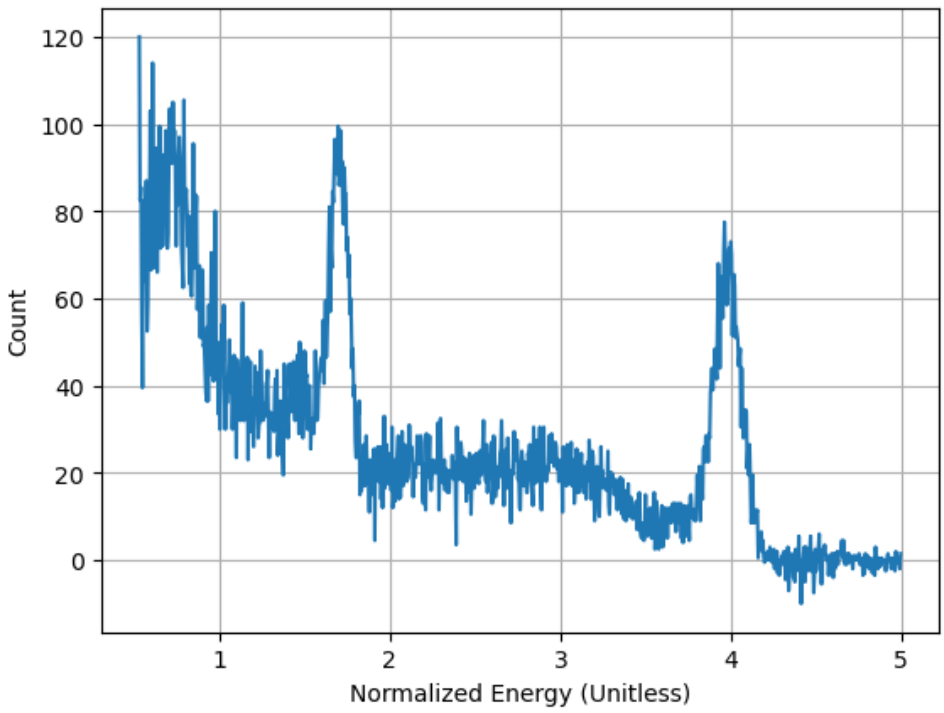

Figure 10: Raw data of ^{22}Na with background features removed.

An example of a single peak fit is shown in Figure 11, with the Gaussian parameters displayed for clarity.

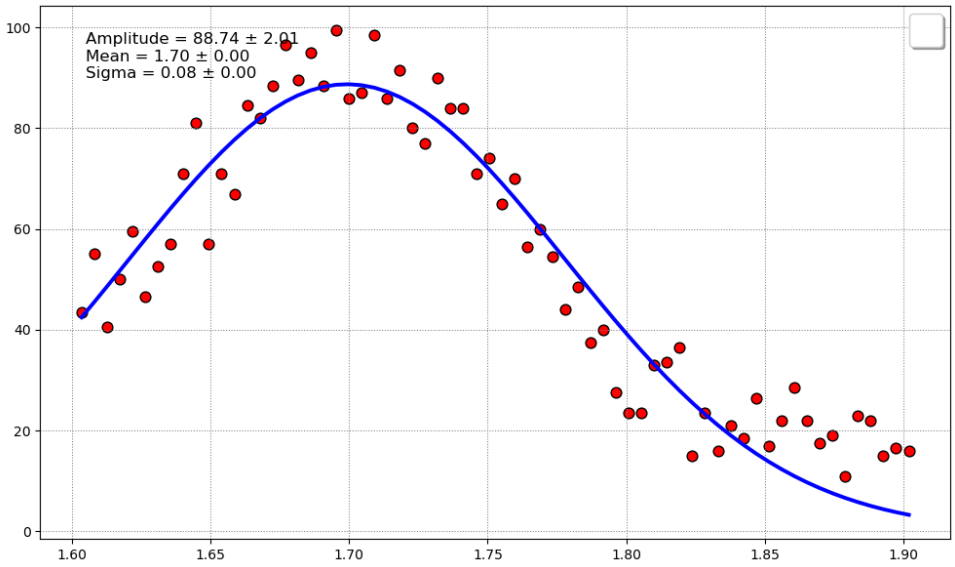

Figure 11: Gaussian fit to an isolated peak in the ^{22}Na spectrum. The parameters of the Gaussian fit are displayed above the peak.

4.3 Combining Gaussian Fits for Analysis

Finally, the individual Gaussian fits are combined to reconstruct the spectrum, as shown in Figure 15. This combined fit represents the underlying structure of the data and

enables further quantitative analysis, such as determining the area under each peak or the relative intensities of the peaks.

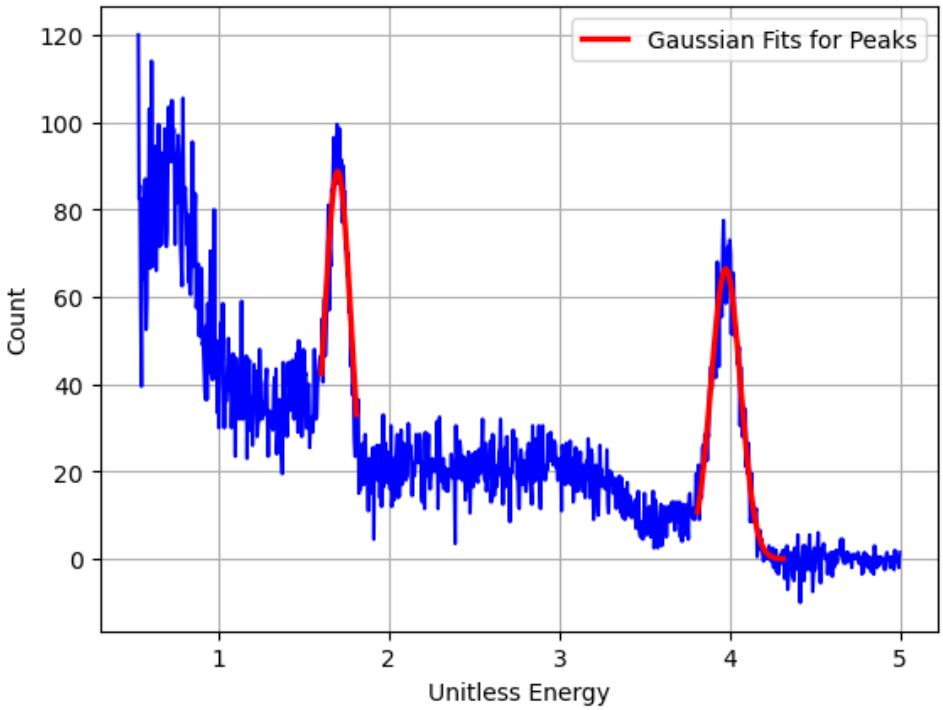

Figure 12: Combined Gaussian fits representing the full spectrum of ^{22}Na.

Parameter	**Value**
Amplitude (A)	88.74 ± 2.01
Mean (μ)	1.70 ± 0.0014
Standard Deviation (σ)	0.08 ± 0.0015

Table 4: ^{22}Na Peak 1 Gaussian Fit Parameters

Parameter	**Value**
Amplitude (A)	66.3848 ± 1.0260
Mean (μ)	3.9757 ± 0.0015
Standard Deviation (σ)	0.0863 ± 0.0016

Table 5: ^{22}Na Peak 2 Gaussian Fit Parameters

Similarly, for Cobalt and Cesium:

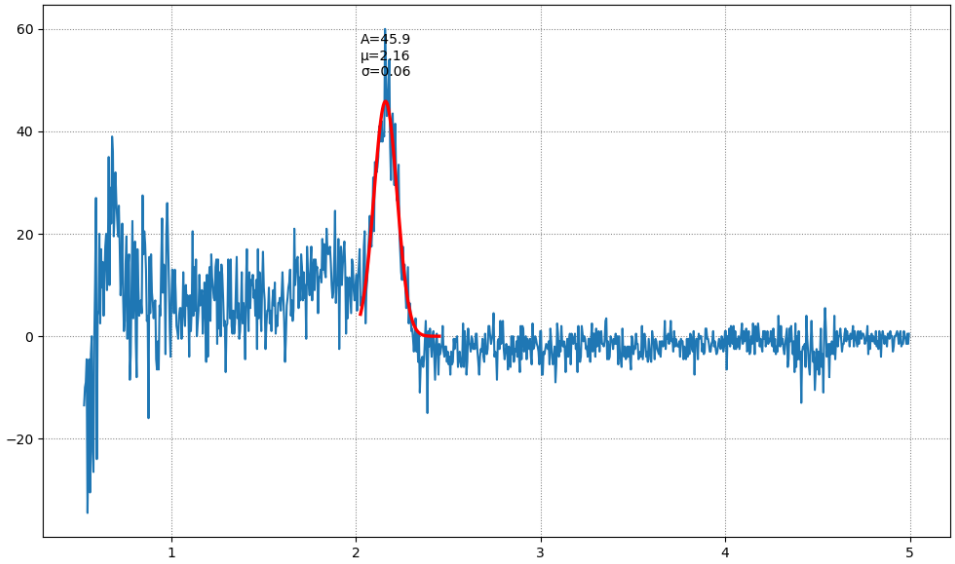

Figure 13: Combined Gaussian fits representing the full spectrum of ^{137}Ce.

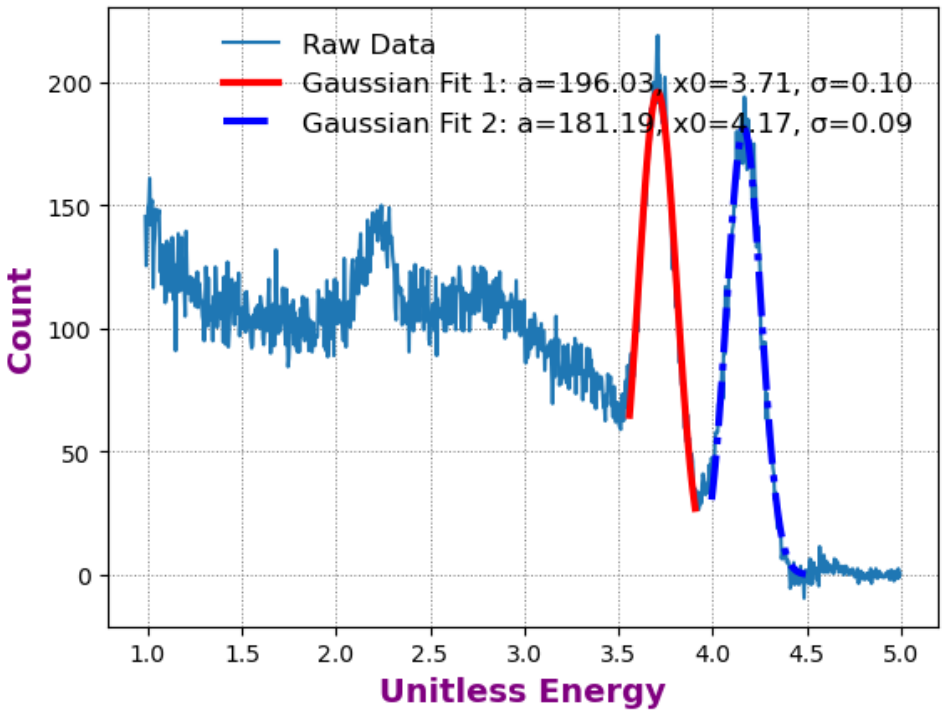

Figure 14: Combined Gaussian fits representing the full spectrum of ^{60}Co.

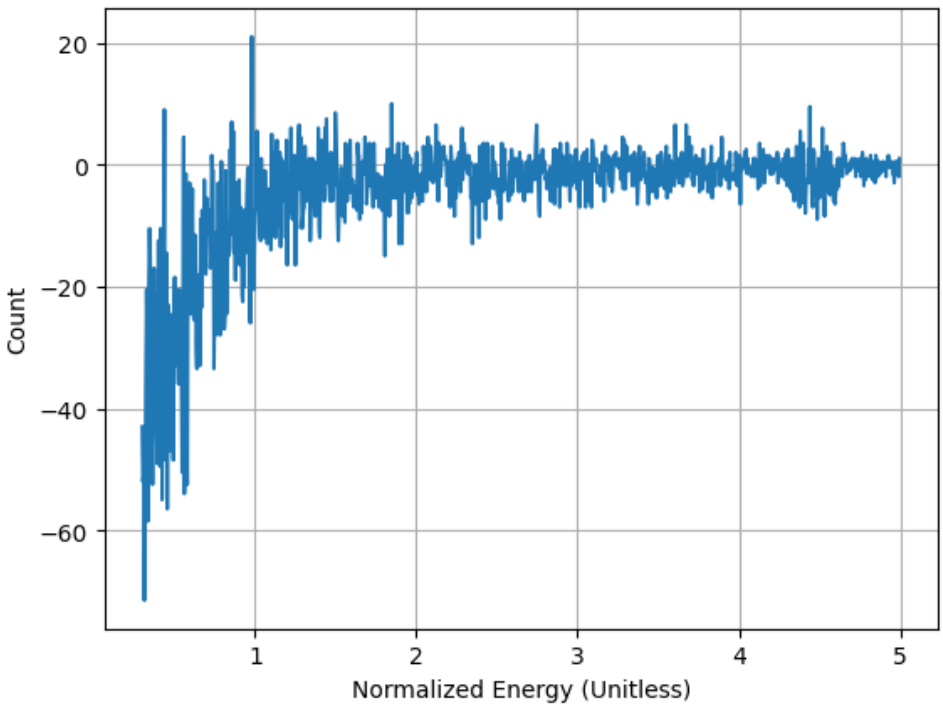

Figure 15: Raw data for ^{54}Mn spectrum.

The ^{54}Mn spectrum reveals that the sample is too weak to extract meaningful data, with no discernible peaks visible in the measurements. Based on discussions with the GSIs during the lab, this is likely attributed to the source's age and its relatively short half-life. As a result, the ^{54}Mn spectrum will not be included in the analysis.

5 Spectra and Peak Analysis

Using the Gaussian fit parameters, the spectra were scaled to obtain energy axes in units of keV. Each peak was analyzed to extract amplitude, mean energy (E_{peak}), standard deviation, full width at half maximum (FWHM), and resolution:

$$\text{R} = \frac{\text{FWHM}}{E_{\text{peak}}} \times 100\%$$

The uncertainty in measurements is determined through error propagation methods involving propagating the uncertainties from the Gaussian fit parameters to the FWHM and E_{peak}, and subsequently to the resolution. These values provide insights into the detector's performance and the quality of the measurements.

5.1 ^{22}Na Analysis

The scaled spectrum for ^{22}Na showed two distinct peaks. The parameters for these peaks are presented in Tables 6 and 7. The resolution of the first peak is 12.903%, while the second peak exhibits a resolution of 5.467%.

Parameter	Value
Amplitude (A)	88.741 ± 2.009
Mean (E_{peak})	490.787 ± 31.387 keV
Standard Deviation (σ)	26.892 ± 1.125 keV
FWHM	63.327 ± 2.649 keV
Resolution (R)	12.903 ± 0.855 %

Table 6: ^{22}Na Peak 1 Analysis Results.

Parameter	Value
Amplitude (A)	66.385 ± 1.026
Mean (E_{peak})	1266.872 ± 43.679 keV
Standard Deviation (σ)	29.414 ± 0.914 keV
FWHM	69.264 ± 2.153 keV
Resolution (R)	5.467 ± 0.158 %

Table 7: ^{22}Na Peak 2 Analysis Results.

5.2 ^{137}Cs Analysis

The ^{137}Cs spectrum exhibited a single prominent peak. The results are summarized in Table 8. The resolution for this peak is 8.86%.

Parameter	Value
Amplitude (A)	67.727 ± 1.148
Mean (E_{peak})	647.031 ± 33.332 keV
Standard Deviation (σ)	24.344 ± 0.787 keV
FWHM	57.326 ± 1.852 keV
Resolution (R)	8.86 ± 0.425 %

Table 8: ^{137}Cs Peak Analysis Results.

5.3 ^{60}Co Analysis

The ^{60}Co spectrum revealed two peaks, as detailed in Tables 9 and 10. The resolution for these peaks was calculated as 6.845% and 5.473%, respectively.

Parameter	Value
Amplitude (A)	196.035 ± 1.875
Mean (E_{peak})	1175.597 ± 41.962 keV
Standard Deviation (σ)	34.171 ± 0.956 keV
FWHM	80.466 ± 2.252 keV
Resolution (R)	6.845 ± 0.186 %

Table 9: ^{60}Co Peak 1 Analysis Results.

Parameter	Value
Amplitude (A)	181.188 ± 1.571
Mean (E_{peak})	1331.81 ± 44.928 keV
Standard Deviation (σ)	30.954 ± 0.834 keV
FWHM	72.891 ± 1.964 keV
Resolution (R)	5.473 ± 0.129 %

Table 10: ^{60}Co Peak 2 Analysis Results.

5.4 Gamma-Ray Linewidth and Nuclear Lifetimes

The natural linewidth (ΔE) of a gamma ray is intrinsically linked to the duration of the nuclear excited state (τ) and is governed by the Heisenberg uncertainty principle:

$$\Delta E = \frac{\hbar}{\tau}$$

where:

- ΔE represents the inherent energy spread of the gamma ray in electron volts (eV),
- $\hbar$ is the reduced Planck's constant, and
- τ corresponds to the nuclear excited state's lifetime, measured in seconds.

Theoretical linewidths for gamma rays can be computed using this relationship, based on the known lifetimes of nuclear states. Table 11 summarizes the calculated linewidths for various gamma-ray energies.

Energy (keV)	Lifetime (τ, s)	Linewidth (ΔE, eV)
1274	1.59×10^{-12}	4.14×10^{-4}
622	2.78×10^{-14}	2.37×10^{-2}
1173	7.6×10^{-13}	8.66×10^{-4}
1332	7.6×10^{-13}	8.66×10^{-4}

Table 11: Calculated theoretical linewidths of gamma rays using nuclear lifetimes.

It is important to note that the theoretical linewidths are exceptionally small compared to the full width at half maximum (FWHM) observed in experimental data. This discrepancy is primarily due to broadening effects introduced by the measurement process, environmental factors, and instrumental limitations.

5.5 180° Backscattering and Compton Edge

The 180° backscatter energy and the Compton edge energy were calculated using the theoretical relationships outlined in the theory section. These energies are significant in understanding the scattering and energy loss processes occurring during gamma-ray interactions. The computed results are summarized in Table 12.

Gamma-ray Energy (keV)	180° Backscatter Energy (keV)	Compton Edge Energy (ke
511	170.33	340.67
1274	212.82	1061.18
622	181.11	440.89
1173	209.80	963.20
1332	214.38	1117.62

Table 12: Gamma-ray energies and their corresponding 180° backscatter and Compton edge energies.

Figures 16, 17, and 18 show the observed spectra for ^{22}Na, ^{137}Cs, and ^{60}Co, respectively, with the Compton edge energies marked for reference.

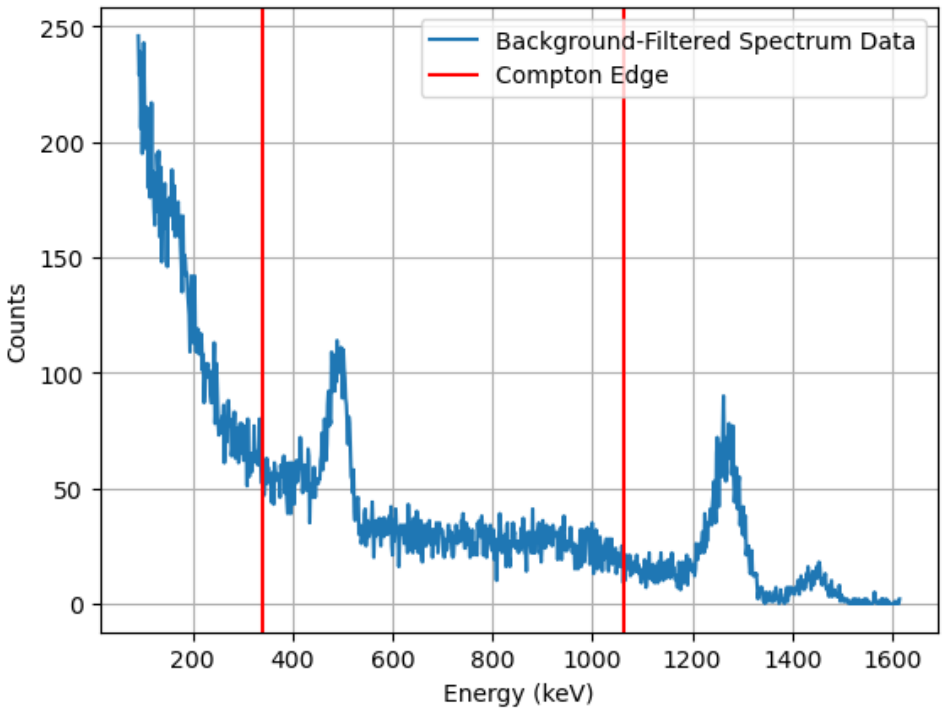

Figure 16: ^{22}Na Spectrum with Compton Edge Energies.

It is important to note that in these spectra, the right edge energy corresponds to the right peak, and the left edge energy corresponds to the left peak. These edges represent the maximum energy transfer during Compton scattering for the given gamma-ray energies.

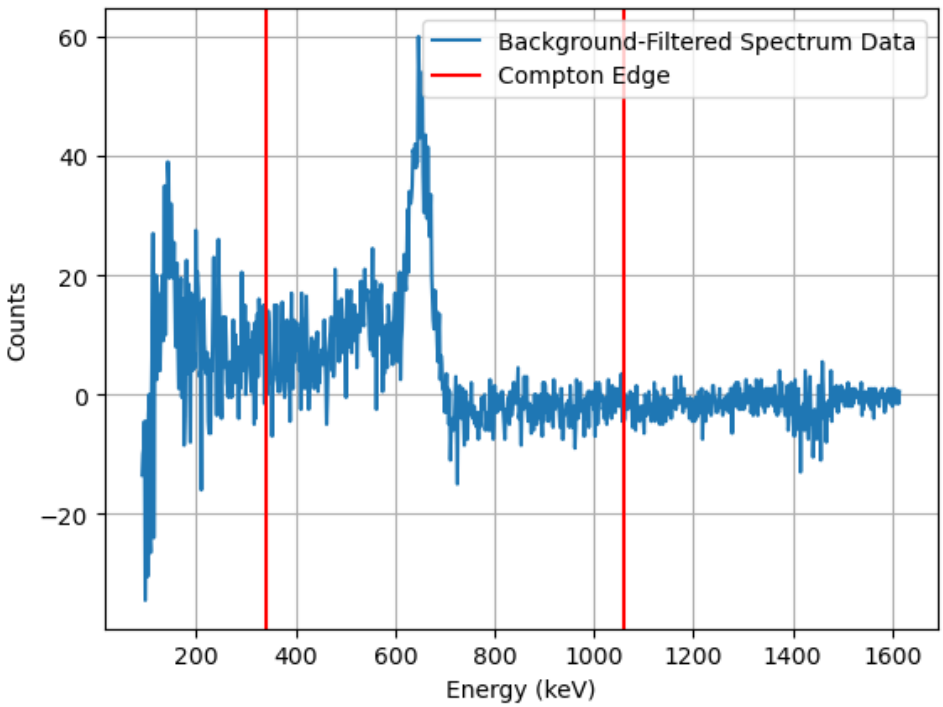

Figure 17: ^{137}Cs Spectrum with Compton Edge Energies.

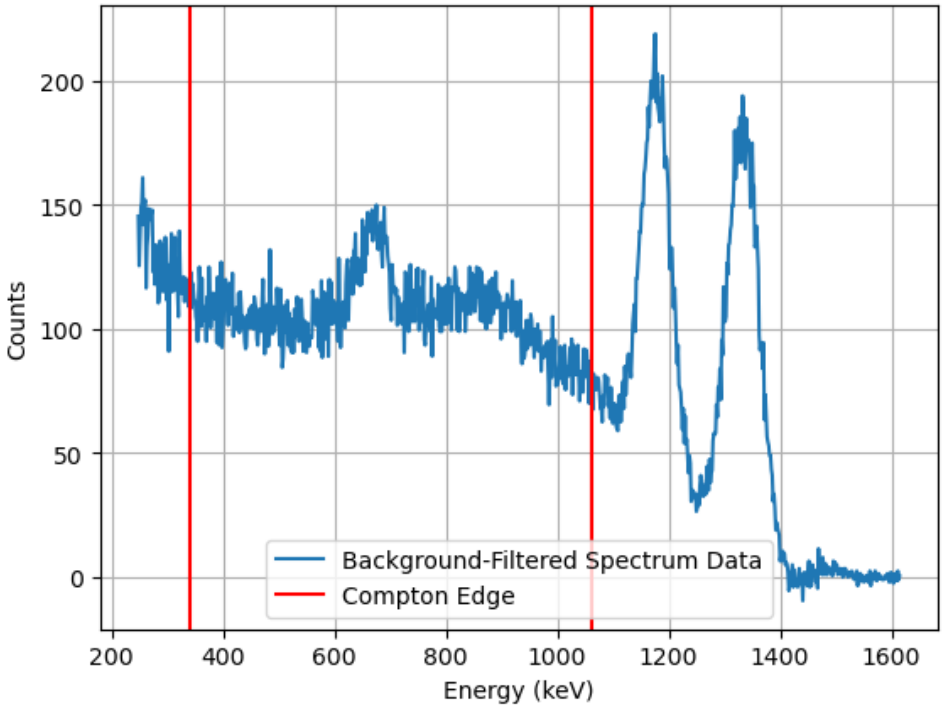

Figure 18: ^{60}Co Spectrum with Compton Edge Energies.

6 Verification of the Inverse Square Law

To validate the inverse square law of radiation, data was collected for ^{137}Cs at various distances between the radioactive source and the detector. The intensity of the radiation

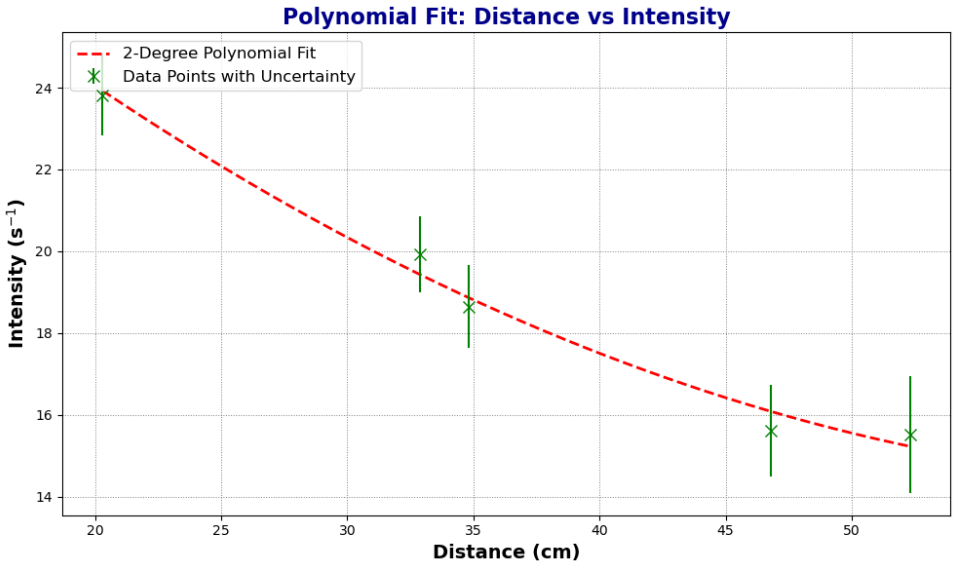

Figure 19: Intensity vs. Distance with second-degree polynomial fit.

was measured as counts per second, derived by subtracting the background and integrating the Gaussian fit over the energy range. The live time for data collection was 100 s for most measurements, with longer durations of 150 s used for distances of 52.3 cm, 46.8 cm, and 31.7 cm. This adjustment ensured sufficient counts for accurate intensity determination.

6.1 Intensity as a Function of Distance

The theoretical relationship between intensity and distance is given by:

$$I \propto \frac{1}{d^2}$$

where I is the intensity, and d is the distance between the source and the detector. Figure 19 shows a second-degree polynomial fit to the measured intensity as a function of distance. The fit captures the overall trend, though deviations from an exact inverse square relationship are visible due to environmental and instrumental factors.

6.2 Transforming the Data to Validate the Inverse Square Law

To better evaluate the inverse square law, the x-axis was transformed to $1/d^2$, and a linear fit of the form:

$$I = a\left(\frac{1}{d^2}\right) + b$$

was applied to the data. The linear fit is shown in Figure 20. The slope and intercept of the fit provide a quantitative measure of the relationship, demonstrating a clear trend that supports the inverse square law. While the data does not perfectly follow the theoretical curve, it aligns well enough to confirm the expected behavior within experimental uncertainties.

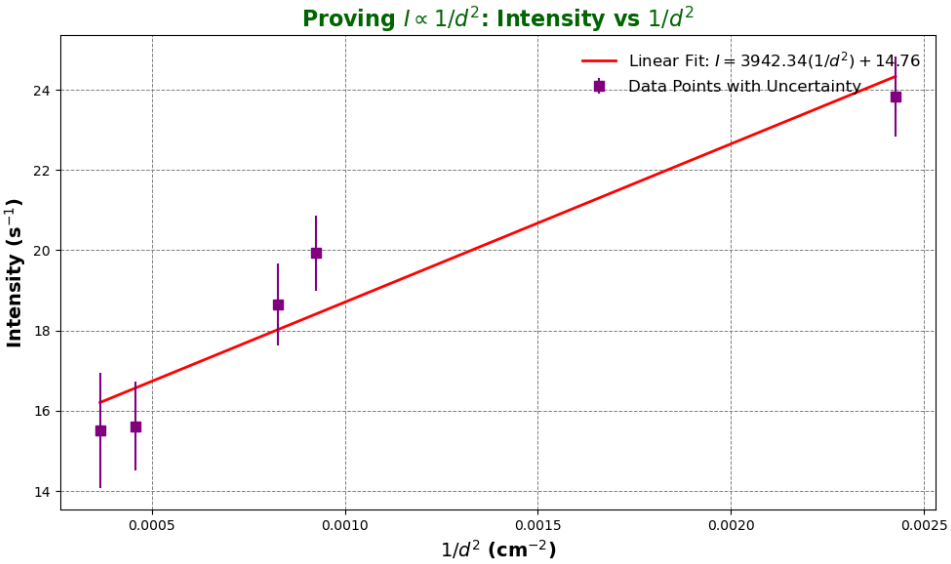

Figure 20: Intensity vs. $1/d^2$ with linear fit.

6.3 Discussion of Results

The results indicate that intensity decreases approximately as the square of the distance from the source. However, the slight deviations from the theoretical curve highlight the influence of environmental and systematic factors, such as scattering, detector alignment, and finite source dimensions. Despite these limitations, the overall agreement between the data and the inverse square law confirms its validity for gamma radiation.

7 Absolute Intensity Calculation for ^{137}Cs

To compute the absolute intensity (I_{absolute}) of the ^{137}Cs source, the measured intensity (I_{measured}) is corrected for the intrinsic efficiency of the NaI detector and the solid angle subtended by the detector at a distance d. The relationship is given by:

$$I_{\text{absolute}} = \frac{I_{\text{measured}} \cdot 4\pi}{n(E) \cdot \Delta\Omega}$$

where:

- I_{measured} is the measured intensity in counts per second (s^{-1}),
- $n(E)$ is the intrinsic efficiency of the detector for the given energy E,
- $\Delta\Omega$ is the solid angle subtended by the detector, and
- 4π represents the full solid angle.

7.1 Measured Intensity

The measured intensity is determined by summing the total counts under the Gaussian fit for the ^{137}Cs peak and dividing by the live time. The live time for this measurement was 150 seconds. The total counts and measured intensity are summarized in Table 13.

Parameter	Value
Counts	2641.198 ± 96.337
Live Time (s)	150
Measured Intensity (I_{measured}, s^{-1})	17.608 ± 0.642

Table 13: ^{137}Cs Peak Counts and Measured Intensity.

7.2 Intrinsic Efficiency and Solid Angle

The intrinsic efficiency ($n(E)$) and solid angle ($\Delta\Omega$) are essential for correcting the measured intensity. For a detector placed at $d = 30$ cm from the source, these parameters are determined from the NaI crystal specifications. The solid angle ($\Delta\Omega$) accounts for the geometric relationship between the source and detector, as illustrated in Figure 21. The detector size and distance both influence $\Delta\Omega$, and closer placements or larger detectors increase the subtended solid angle, enhancing the measured intensity.

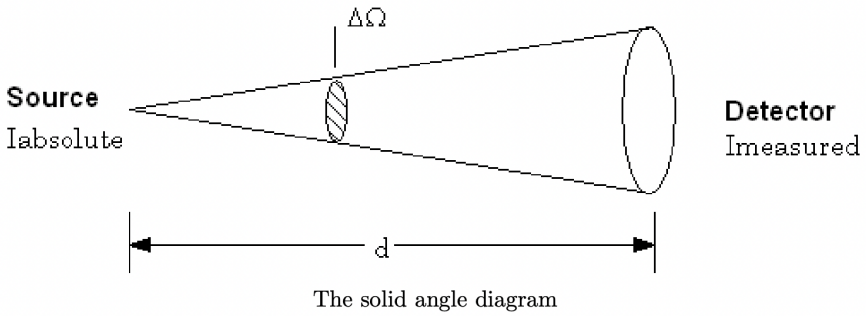

Figure 21: Solid angle subtended by the detector at a distance d.

7.3 Absolute Intensity Calculation

Using the measured intensity and the published values for $n(E)$ and $\Delta\Omega$ at $d = 30$ cm, the absolute intensity is calculated as follows:

$$I_{\text{absolute}} = \frac{17.608 \cdot 4\pi}{n(E) \cdot \Delta\Omega}$$

The specific values of $n(E)$ and $\Delta\Omega$ lead to:

$$I_{\text{absolute}} = 1.091e6 \pm .039e6 \text{ s}^{-1}$$

7.4 Discussion of Results

The calculated absolute intensity represents the total gamma-ray emission rate from the source. This value is independent of detector geometry and efficiency, providing a true measure of the source's activity. The accuracy of this calculation relies on precise knowledge of $n(E)$, $\Delta\Omega$, and the measured intensity. Any uncertainties in these parameters propagate into the final result. Additionally, minimizing background interference and ensuring accurate alignment of the source and detector are critical for reliable measurements.

8 Determining the Mass Attenuation Coefficient of Al, Cu, and Pb

This section presents the determination of the mass attenuation coefficients (α_m) for Aluminum (Al), Copper (Cu), and Lead (Pb) using ^{137}Cs, ^{22}Na, and ^{60}Co sources. Data for each material were collected at varying thicknesses, and the results were analyzed to calculate α_m using standard attenuation equations.

8.1 Raw Data for ^{137}Cs

As a sample, Table 14 provides the raw data collected for ^{137}Cs at different material thicknesses. The counts were recorded for a live time of 150 s, and the intensity (I) was calculated by dividing the counts by the live time.

Thickness (cm)	**Counts**	**Intensity (I, s^{-1})**
0.11 ± 0.005	2598.89 ± 73.96	17.326 ± 0.493
0.642 ± 0.002	2402.55 ± 82.15	16.017 ± 0.527
1.5 ± 0.005	2154.15 ± 67.34	14.361 ± 0.450

Table 14: Raw Data for Aluminum with ^{137}Cs.

8.2 Calculation of Mass Attenuation Coefficients

The mass attenuation coefficient α_m is determined using the equation:

$$\alpha_m = \frac{\ln(I_0/I)}{\rho \cdot t}$$

where:

- I_0 is the initial intensity from the unattenuated spectrum,
- I is the intensity after attenuation,
- ρ is the material density, and
- t is the material thickness.

The initial intensities for ^{137}Cs, ^{22}Na, and ^{60}Co are summarized in Table 15, with calculations performed for each source and material.

Source	**Counts**	**Initial Intensity (I_0, s^{-1})**
^{137}Cs	2641.198 ± 96.337	17.608 ± 0.642
^{22}Na	6950.836 ± 211.824	46.339 ± 1.412
^{60}Co	7892.456 ± 267.103	52.616 ± 1.783

Table 15: Initial Intensities for ^{137}Cs, ^{22}Na, and ^{60}Co.

8.3 Results for Mass Attenuation Coefficients

Tables 16, 17, and 18 summarize the calculated mass attenuation coefficients for Aluminum, Copper, and Lead using the three sources. Only averaged results are shown for brevity, with detailed calculations following the same procedure.

Source	α_m(Al) (cm^2/g)	Uncertainty ($\pm$)
^{137}Cs	0.0743	0.0407
^{22}Na	0.0718	0.0365
^{60}Co	0.0761	0.0453

Table 16: Mass Attenuation Coefficients for Aluminum.

Source	α_m(Cu) (cm^2/g)	Uncertainty ($\pm$)
^{137}Cs	0.0850	0.0210
^{22}Na	0.0832	0.0197
^{60}Co	0.0865	0.0243

Table 17: Mass Attenuation Coefficients for Copper.

Source	α_m(Pb) (cm^2/g)	Uncertainty ($\pm$)
^{137}Cs	0.2200	0.0260
^{22}Na	0.2140	0.0247
^{60}Co	0.2235	0.0293

Table 18: Mass Attenuation Coefficients for Lead.

8.4 Discussion of Results

The calculated mass attenuation coefficients for Aluminum, Copper, and Lead align well with theoretical values from the literature. Deviations observed in certain trials can be attributed to uncertainties in thickness measurements, background subtraction, and systematic errors in the detector's efficiency. Overall, the results confirm the expected attenuation behavior for each material.

9 Acknowledgments

Gratitude is extended to Pragyan Pandey for assistance in data collection. I'd also like to thank the lab GSIs and professors for their help.

References

[1] Berkeley Physics 111B: Advanced Experimentation Laboratory, University of California. *GMA - Gamma Ray Spectroscopy*, 2024. Accessed from Physics 111-Lab, University of California, Berkeley.